Considerations for a 3D super-resolution interferometric microscope in biology

Mark Ransley

Supervisors: Phil Jones & Geraint Thomas
University College London
m.ransley.12@ucl.ac.uk

Abstract

In this report we address the need for a new type of microscope in biological metrology, and consider means of extending an existing sub-nanometric interferometry measurement system into a 3 dimensional non-invasive instrument for surface profiling and volumetric study. We note that such a device would require algorithmically solving an inverse problem to extract the sample structure from the captured interferograms, and examine various modelling techniques that could be used in formulating the inverse problem.

I. Introduction

Visible light optical microscopy has been a key tool in biological discovery and understanding for centuries, however the resolution of the traditional microscope is limited by the diffraction of light [1]. It was shown by Ernst Abbe that light could be focused to a point of radius

$$d = \frac{\lambda}{n \sin \theta}$$

where λ is the wavelength, n is the refractive index of the medium and θ is the angle at which the focusing converges. Thus features within this radius are indistinguishable.

In biology many structures of interest are smaller than the diffraction limit, so the study of such crucial topics as virus architecture, membrane transport and molecular mechanics relies on super-resolution technology. There are many methods for overcoming the diffraction limit, the most popular of which are discussed here and depicted in figure 1, though they are all beset with difficulties that render them unsuitable for various important biological observations.

Scanning Electron Microscopy (SEM) emits a beam of electrons whilst scanning the sample surface, and the detected scattering of electrons and emission of x-rays are used to construct an image of the surface topography [2]. At typical SEM voltages, electrons have a de Broglie wavelength of 12.2 pm [3], and changes in the surface profile of the order nanometers can be detected. To prevent artefacts resulting from the electrons colliding with air, SEM must be conducted inside a vacuum, which in return requires that the sample be fixed either with chemicals such as formaldehyde or through freezing (cryo-SEM) [2]. This prevents the investigation of dynamical processes. Additional techniques are available to investigate the interior of cells - 'freeze fracturing' is a means of breaking the cryo-preserved specimen open, enabling study of the internal structure [4]. Environmental SEM operates under atmospheric pressure and humidity, albeit with lower contrast [5].

Transmission Electron Microscopy (TEM) is used to obtain images of very thin cross sections of a sample. By rotating the beam of emitted electrons about the specimen, a series of cross sections can be taken and then composited into a 3D image. In 2012 Scott et al. [6] used this method to survey a gold nano-

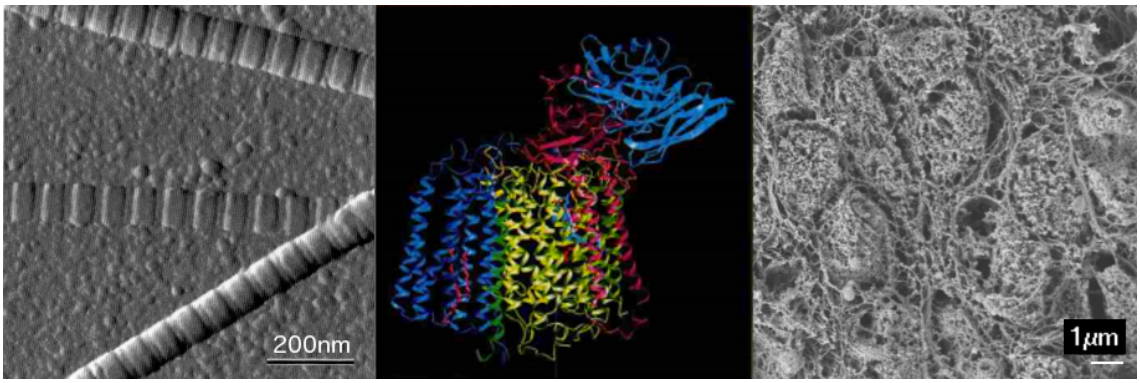

Figure 1: *Biological images obtained through* ***(a)*** *AFM; variable deflection image of collagen fibres from [8],* ***(b)*** *x-ray crystallography; cytochrome c oxidase membrane protein complex from [14],* ***(c)*** *SEM; cross section on gut muscle, taken at UCL*

particle at 2.4Å. Since the slices must be at most of order μm thick for successful transmission of electrons [7], biological matter must again be preserved, usually in epoxy resin, prior to slicing.

Atomic Force Microscopy (AFM) rasters a cantilever with nanometric tip across the sample surface, and a laser beam is deflected from the top to indicate surface displacements and small forces such as van der Waals and electrostatic [8]. Longitudinal (z) sensitivity is dependent on the photodetector accuracy, but can be as low as 100pm, whilst x and y resolution is determined by the raster scanning system employed. Usually this is a set of Piezo transducers, allowing for sub-nanometric scan increments. Due to the tip geometry AFM is unable to resolve certain types of feature on the sample surface.

For the imaging at the atomic level, x-ray crystallography has long been used for resolving molecular structures. If possible, a crystal lattice of the substance in question is formed and then bombarded with x-rays radiating from a synchrotron. X-rays passing through the lattice are diffracted by electrons, and an electron density map can be calculated from the transmitted field. From this the location of atoms may be inferred, and entire macromolecular models can be produced [9]. In biology this technique has been used to image a plethora of structures, including numerous proteins and protein complexes, amino acids, peptide-presenting membrane molecules and viruses [14]. However since an individual molecule does not produce detectable amounts of x-ray diffraction, formation of a well ordered lattice is an essential (and often very difficult) requirement for x-ray crystallography.

Confocal microscopy [15] combines optical techniques with fluorescence to obtain high quality 3D images of specific biological components. Fluorescent molecules, often proteins are attached to cellular constituents and a laser is shone through a pinhole and focused accurately to a point in 3D space. Photons emitted by the fluorescent specimen are then recorded for that point, and raster scanning is used to build up a tomogram. Adjustment of the focal plane then allows for multiple optical sections to be compiled into a volumetric recording. By tagging various compounds with different fluorescent probes, the interaction between biological entities can be studied, and due to the fast rates of scanning and focusing, realtime volumetric videos can be captured. However, since fluorescence occurs for visible light, confocal microscopes are diffraction limited.

Stimulated Emission Depletion (STED) [1] employs two laser pulses, one to excite the fluorescent molecules within the focal point, followed immediately by a circular pulse, generated using a higher mode of cavity resonance, to deactivate fluorescence, leaving a smaller

region of photon emission than a standard focussed beam would allow. Techniques such as STED can thus be used to bypass the diffraction limit, but depend on fluorescent tags, which are often large compared to their host and must be carefully chosen depending on the investigation [16].

It should be noted, at the end of this technology review, that all of the super-resolution microscopy techniques considered require digital post-processing of the captured data to create the desired output. With x-ray crystallography in particular the entire structure must be solved computationally, whilst scanning based instruments capture vast arrays of individual measurements, which may then be converted into images such as the ones shown in figure 1.

An ideal biological microscope for addressing today's problems would be capable of sub diffraction-limited resolution, both for determining surface topography and interior makeup of live specimens, without the need for dyes or fluorescent tags.

II. Interferometry

Around 1801 physicist Thomas Young showed that light was indeed a wave, corroborating theories of Hooke and Huyghens and contradicting the highly regarded particle theory of Newton. Young's famous double slit experiment illustrated how two sources of light interfere, giving rise to periodic magnification and cancellation of intensity when both sources illuminate a screen. The observed set of fringes (see figure 2), henceforth known as an interferogram, were due to the two light fields being in and out of phase with each other across the spatial domain. The theory of interference was developed further by Fresnel and a new metrological science of interferometry was formed. Notable applications of interferometry have included the Michelson-Morley experiment, which disproved the existence of a luminiferous aether through which light was assumed to propagate, the measurement of the wavelength of ^{86}KR radiation, from which the exact definition of the metre was defined, and the measurement of the diameters of Jupiter's satellites by Michelson in 1890 [17].

Many types of interferometer have been developed, but the two of most interest to us in this report are the Michelson and Mach-Zehnder devices. A Michelson interferometer works by passing light through a beam splitter. Half is propagated along a "reference arm" incident to a mirror, whilst the other half is propagated along a "measurement arm", identical except the path length is altered by the mirror being longitudinally displaced (producing an interferogram akin to figure 2a) or tilted (2b). Both beams are reflected back to the splitter, where they are recombined and together reflected onto a screen. More recently a charge coupled device (CCD) would be used as a photodetector so that interferograms may be processed and stored digitally, and the light source of choice would be a laser due to its monochromatic, spatially coherent output [22]. It is possible that instead of a mirror, the measurement beam could be reflected from a biological surface [11], effectively an array of slightly reflective surfaces with varying displacements and tilts. Information about the surface would then be contained in the interferogram, though interpretation of the results may prove complicated and will be discussed in Section IV.

The Mach-Zehnder device is similar to the Michelson, but the measurement arm accumulates changes in phase due to passing *through* samples, thus being temporarily slowed down or sped up due to the change in refractive index. Diagrams of Michelson and Mach-Zehnder instruments are given in [19].

As a simple model, we consider a wave represented in the following complex form:

$$E(\mathbf{x}, t) = E_0 e^{i(\mathbf{kx} - \omega t)} \tag{1}$$

where $\mathbf{x} = (x, y, z)$, E_0 is the initial energy, $\mathbf{k}$ is the wave-vector such that $|\mathbf{k}| = \frac{2\pi}{\lambda}$ and ω is the period. The phase is defined as $\phi = \mathbf{kx} - \omega t$, and rewriting (1) in terms of ϕ reveals the property that $E(\phi) = E(\phi + 2\pi)$. Figure 2a is the radial fringe observed when two waves E_1 and E_2 with a longitudinal offset are interfered. This is the type of image

produced in a Michelson interferometer when the measurement beam has travelled a longer or shorter path than the reference beam. To model this we evaluated E_1 across a grid of x and y values, holding $z = z_1$ constant, and then repeated the evaluation for E_2 with $z = z_1 + \delta$, a small displacement. The intensity is given by $|E_1 + E_2|$. The linear fringes of Figure 2 were obtained by offsetting x instead of z, and are the type observed in a Michelson interferometer when the measurement mirror is tilted.

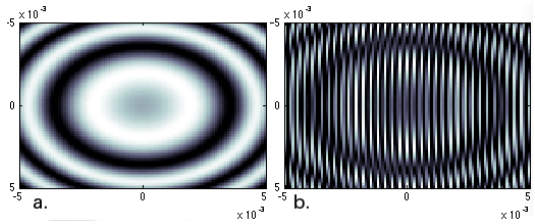

Figure 2: *Interference fringes simulated for* ***(a)*** *longitudinal (z) and* ***(b)*** *transverse (x) displacements.*

The above toy model provides numerical verification of the diffraction limit, where displacements $< \lambda/2$ produce no discernible difference.

Algorithms exist to determine the change in distance through fringe counting [29] [21], though as we shall see later these are not applicable to the irregular sample surfaces we are interested in.

Since a change in distance corresponds to a change in phase ϕ, which in turn gives rise to the change in intensity, there is an ambiguity in that $\delta = \delta + n\lambda$ for any integer n; the so called 2π ambiguity. We propose this could be avoided by using two wavelengths,

$$\lambda_2 = \frac{a}{b}\lambda_1$$

where a and b are coprime, and $b - a$ is small, in order to keep both wavelengths in the visible range. Thus the first ambiguity for both measurements occurs at distances of $b\lambda_2$. By choosing b to be large, we can move ambiguities far outside our range of concern. This technique uses a synthetic wavelength to effectively multiply the measurement wavelength and extend the range of discernible distances. Similar methodology can be used to subdivide the wavelength, achieving greater than diffraction-limit sensitivity. In the most impressive example, Chen et al. [23] used a synthetic wavelength to measure longitudinal displacements as little as 50pm. The remainder of this report will consider using this technique to achieve super-resolution microscopy.

III. Subdivision by Synthetic Wavelength

The Chen interferometer was described in some detail in [19] and so will only be covered briefly here. To summarise its workings, two orthogonally polarised beams of wavelengths λ_1 and λ_2 were sent together across a path of length L, which was adjustable by length ΔL, and then recombined with the initial beams accumulating phase differences $\phi_1 = 2\pi(L + \Delta L)/\lambda_1$ and $\phi_2 = 2\pi(L + \Delta L)/\lambda_2$. Using a polarising beam splitter, one arm of the second beam was partially allowed to travel an additional distance L_2 to a measurement corner cube (MCC), where sub-nanometric distance changes Δl_2 occurred. The difference in phase change between the two beams was thus given by:

$$\begin{aligned}\Delta\phi' &= \phi_1 - \phi_2 \\ &= 2\pi\left(\frac{L+\Delta L}{\lambda_1+} - \frac{L}{\lambda_2} - \frac{L_2+\Delta l_2}{\lambda_2}\right) \\ &= 2\pi\left(\frac{L+\Delta L}{\lambda_s} - \frac{L_2+\Delta l_2}{\lambda_2}\right)\end{aligned}$$

where the synthetic wavelength $\lambda_s = \lambda_1\lambda_2|\lambda_1 - \lambda_2|$. The change in path length ΔL was then varied until $\phi' = 0$, at which point it holds that

$$\Delta l_2 = \frac{\lambda_2}{\lambda_s}\Delta L \tag{2}$$

Wavelengths are known, therefore Δl_2 can be determined by measuring ΔL. Since $\lambda_s >> \lambda_2$, a sub-nanometric change in Δl_2 corresponds to a millimetre scale change in ΔL. In [23] this theory and the claimed sensitivity were experimentally verified by moving the MCC with a piezo transducer.

As a proof of concept, this method is remarkable. However a number of issues prevent it from being directly applicable to biological microscopy. The instrument currently only detects one dimensional displacements at a single point, so could be used as a scanning probe. We propose the measurement beam could be propagated along fibres within a cantilever, and thus used as a far more compact alternative to traditional AFM (figure 3). However, issues with AFM have been discussed and light, being far less invasive, would be a preferable probe to the cantilever tip. Hence we shall continue to consider means of reconciling the pico-scale resolution of synthetic wavelength interferometry with optical microscopy.

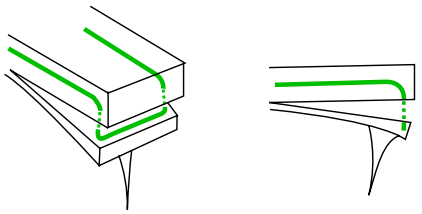

Figure 3: *A proposed modification of the Atomic Force Microscope cantilever tip using the measurement beam from the system devised by Chen*

Interferometers are extremely sensitive to external disturbances, and should therefore be robustly constructed, contained within one unit, and have as few mechanical parts as possible. Making macro-adjustments to the distance ΔL for every measurement would prove time consuming and possibly send disruptive vibrations to crucial points in the system, given the minuscule length scales involved. Hence we suggest using an electro-optic modulator (EOM) to directly change the phase without any need for increasing optical path, a method previously explored in [18]. EOMs are materials, generally crystals, where the refractive index depends on the surrounding electromagnetic field. Δl_2 could thus be determined from the voltage required to induce a change in phase such that $\Delta\phi' = 0$.

Assume for now a sample surface behaves as an array of flat reflective pixels of varying elevation (call this the "Lego-brick assumption"). If the measurement beam of the Chen interferometer were directed obliquely at the surface rather than through the MCC, the resulting difference interferogram (Intλ_1 − Intλ_2) would contain information about the height of every point illuminated by the beam. However, under Chen's method extracting this information would require adjusting ΔL for each point. This could be accomplished simultaneously using a spatial optic modulator, a matrix of EOMs similar to an LCD screen [27]. However these devices are expensive. Using a single EOM the phase could be modulated so that $\Delta\phi'_{x,y} \to 0$ for each pixel consecutively, though this would involve the instrument being operated for a long time to capture each image - ideally structure inference would be carried out in post-processing.

Under the Lego-brick assumption, the above methods could be used to achieve pico-scale resolution along the z axis. However, transverse resolution is still diffraction limited and Airy disks would form. One solution would be to use two orthogonal measurement beams orientated at an angle θ_i to the sample. In [19] Wyatt described the smallest observable step as a function of the incident and collection angles. There is a risk of signal from one beam being collected by the lens/CCD of the other, so we suggest using separate wavelengths in each head. This would render the interferograms source specific, since light of different wavelengths cannot interfere.

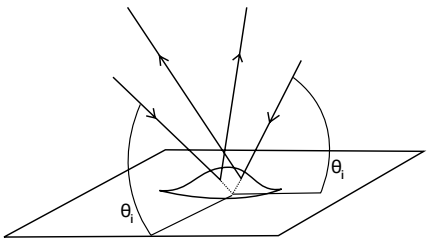

Figure 4: *Biaxial probe*

In an isometrically illuminated system such as this, rays would no longer be incident at 90°, and the elevation at each lateral coordinate could no longer be determined from a single

corresponding phase modulation. The question arises of how one could extract information about the sample from the two difference-interferograms. At this point the surface geometry would have to be considered as an inverse problem.

IV. Inverse problems

By modelling the entire system of beam interactions with the sample surface, the surface geometries could be optimised so that the simulated difference-interferograms correspond to those observed. This is similar to the work of UCL's Prof. Simon Arridge at the Centre for Medical Image Computing, and belongs to the class of inverse problems. Techniques for modelling the beams and reflections will be discussed in the next section. To begin with we will consider purely reflective surfaces, though as the final chapter suggests, it may be possible to obtain information through the sample's entire volume.

Due to the potentially very large parameter space, a genetic algorithm seems a suitable choice for optimisation engine. Such an algorithm borrows the principles of crossover and mutation from nature in order to iteratively evolve a diverse population of random guesses to a satisfactory solution. To investigate this, we considered the simple case of a Michelson interferometer obliquely illuminating a biological sample with a Gaussian beam. The Lego-brick assumption was employed to ensure that each point in the sample arm reflected the light directly back to its source. Without this, the gradient in x and y of each surface pixel would have to be taken into account, trebling the number of parameters needing to be optimised. As an initial test, the sample was a 20x20pixel section from a cell surface map, with elevation span 6nm. Using a population of size 40, the optimisation was programmed to continue for no more than 1000 generations which took around 15 minutes on a dual core CPU, resulting in the inferred elevation profile shown alongside the original surface in figure 5. The normalised error was 8.51E-4. Many more evolutionary parameters were utilised than those mentioned in the algorithm description, so it is very likely the performance could be improved with tweaking.

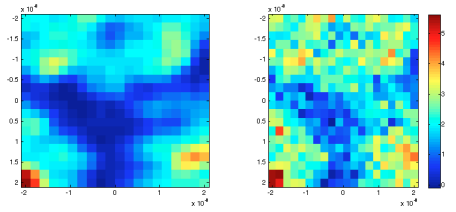

Figure 5: *Simulated interferogram for a 20x20pixel surface profile of a cellular interface.* ***Left*** *was generated from the actual profile, whilst* ***Right*** *was formed from optimising surface geometries. The colour bar ranges from 0-6nm*

When working with larger resolutions we suggest beginning by scaling down the interferogram to a very low resolution, then using the optimised surface as a basis for the initial population of a slightly higher resolution attempt. Through this iterative approach the vast parameter space is restricted to more reasonable values.

V. Gaussian beams

Lasers are ideal for interferometry as they emit monochromatic, spatially coherent (i.e. emissions at any two points along the beam of propagation are able to interfere) light [22]. Operating in the fundamental TEM_{00} mode they are best modelled as Gaussians [20]. Such beams propagate along the z axis, and the beam width about this axis diverges from either side of the 'waist' (figure 6).

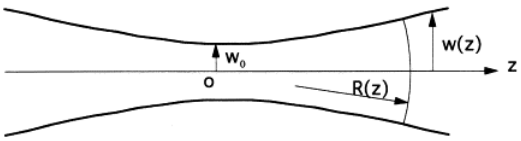

Figure 6: *Longitudinal profile of a Gaussian beam. Taken from [10]*

The equation for a Gaussian beam [24] is given by (3), page 7, with components explained below.

$$E(r,z) = E_0 \frac{w_0}{w(z)} exp\left(\frac{-r^2}{w^2(z)} - ikz - ik\frac{r^2}{2R(z)} + i\xi(z)\right) \quad (3)$$

r is the radial distance from the beam axis, defined as $r = \sqrt{x^2 + y^2}$.

E_0 is the initial (maximum) energy.

w_0 is the width of the waist of the beam, occurring at $z = 0$.

$w^2(z) = w_0^2\left[1 + \left(\frac{z}{z_R}\right)\right]$

$z_R = \frac{\pi\omega_0^2}{\lambda}$ is the Rayleigh range, the distance at which $w(z) = \sqrt{2}w_0$.

$R(z) = \frac{(z^2+z_R^2)}{z}$ is the radius of curvature of phase fronts.

$\xi(z) = -\arctan(z/z_R)$ is the Guoy phase shift, a term that provides a phase shift of π when the beam passes through a focus.

V.1 Rotations and Transformations

The Gaussian beam model propagates along the z-axis, with radial width in each (x, y) cross section. In scenarios where the beam is being manipulated through reflection or refraction, the direction of propagation will change in accordance with the incident angle θ_i. The beam could be defined as moving along a vector $\boldsymbol{k}$ instead of z, with the radius always occurring in the plane orthogonal to $\boldsymbol{k}$. However for basic systems (only one transformation) it is easier to work in terms of coordinate transform matrices. There are two coordinate systems available, inert (lab), where the direction of the beam is perceived to change, and spatial (beam) coordinates, i.e. those from the beam's perspective, the direction of propagation remains constant. In 2D, transferring between lab and spatial frames requires pre-multiplication of the spatial coordinates (ie. how far along the z-axis and the outward radius) by the following special orthogonal matrix:

$$T(\theta) = \begin{bmatrix} \cos(\theta) & \sin(\theta) \\ -\sin(\theta) & \cos(\theta) \end{bmatrix}$$

where θ is the angle of the beam in the (x, z) plane ($\theta = 0$ implies motion along the z-axis, as indicated by $T(0) = Id$). Being an orthogonal matrix, $T^{-1} = T'$, so beam coordinates may be switched back to lab ones through pre-multiplication by T'.

(x, z) transformations of the beam can also be achieved. To centre the beam waist at (x',y',z') instead of (0,0,0), the beam intensity function must be evaluated at (x-x',y-y',z-z').

When evaluating the beam intensity across an area in the lab frame, changes to the wave vector by reflective surfaces etc. can be simply modelled by evaluating the incident wave only up to the point where transformation occurs, then evaluating the transformed wave across relevant space thereafter. It should be noted that on reflection a beam goes through a phase shift of π [12].

This type of method is very inefficient for complex light based simulations. In the final chapter we will discuss the use of ray-tracing as an alternative.

VI. Modelling the synthetic wavelength interferometer

We wish to extend the Michelson interferometer based inverse problem outlined in Section IV to one capable of determining sub-nanometric changes in surface profile. This is in fact hardly any more computationally intensive than the basic problem. There would be no need to vary the reference arm, but rather to vary the surface geometry to produce the intensity-difference-interferogram (IDI).

In the dual-axial system, a change in one surface geometry parameter would usually correspond to two changes in output; the IDI for each interferometer, thus aiding the optimisation by removing ambiguity.

In Chen et al. it is given that $\lambda_1 = 632.8\text{E} - 4$ and the frequency difference between the two waves is $\Delta\nu = 1078462255$. Thus λ_2 can be

calculated as

$$\lambda_2 = \frac{c}{\frac{c}{\lambda_1} - \Delta\nu}$$

An additional two wavelengths may be required for the second probe, as suggested in Section III.

For a given length L, the first interferogram $Int\lambda_1$ is a constant throughout the problem. For each potential surface profile, $Int\lambda_2$ must be generated as a function of surface elevation, and the $IDI = Int\lambda_2 - Int\lambda_1$ compared to the observed difference interferogram. This must then be repeated for data captured from the second probe.

VII. Feasibility of the dual-wavelength, bi-axial inverse problem with gradients

Whilst the Lego brick assumption may hold for certain manmade nanoscale objects, it clearly will not apply in reality to biological surfaces. For a completely reflective surface, there are three parameters to be considered for every point in the surface's x-y grid; height of surface, x-gradient and y-gradient, resulting in unwieldy numbers of parameters. For example, a relatively small 201x201 surface amounts to 121,203 parameters. However, restricting each height to greater than 0 and restricting the gradients to integers would aid the genetic algorithm, which itself can be run on parallel processors. For each generation of the genetic algorithm, a population of a given size n, corresponding to n potential surface geometries, is evaluated. Fortunately, each member of the population can be considered independently of the others, with fitness values being compared afterwards, allowing for the evaluation to be run on a parallel cluster. As mentioned previously, iterating up from low resolution approximations would greatly increase the efficiency of the algorithm. A cluster of graphical processing units would be well suited to this computation as it is similar to the ray tracing calculations they excel at. It should also be noted that the image processing does not have to be especially rapid provided the inverse problem is solvable, since the IDI images can be captured in real time, then stored and processed to generate the surface profile later, and that it is commonplace for supercomputer problem solving to last for days.

VIII. Interior microscopy

So far we have considered the synthetic wavelength interferometer as a system of Michelson interferometers, where light from the measurement arm is reflected from the sample to create subdivided fringes. However a Mach-Zehnder interferometer could also be used if light were allowed to pass through the sample, and be collected underneath. It would be possible to construct a bi-axial super-resolution device consisting of both Michelson and Mach-Zehnder interferometers, where the Michelson components measure back-scattered light and the Mach-Zehnder measure transmitted light (figure 7).

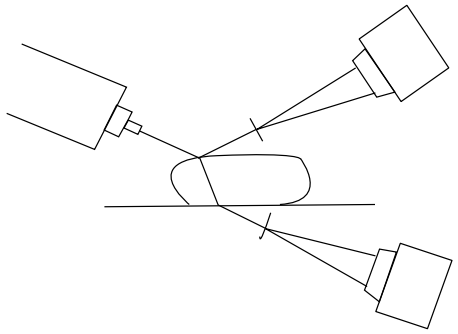

Figure 7: *Schematic of a dual mechanism interferometer for measurement of reflective and refractive properties.*

Mechanically the device would only require little more than one additional CCD per beam, since the same reference beam system would be used to form IDIs for both reflected and refracted light. As an inverse problem, this would be vastly more complicated, since there is no longer one surface to be optimised but an entire volume. Each voxel would require a refractive index, x and y gradients, and an absorption coefficient. Rates of transmission and reflection would be computed at each voxel

interface according to Fresnel's equations, and angles calculated by Snell's law. To aid the genetic algorithm further, the refractive indices for various living tissue components are given in Table 1. It is clear from the table that internal points are likely to have refractive indices lying between 1.35-1.53, though there may be other components in the sample with values lying outside this range.

Tissue component	Refractive index
Interstitial fluid	n = 1.35-1.36
Cytoplasm	n = 1.36-1.375
Nucleus	n = 1.38-1.41
Mitochondria	n = 1.38-1.41
Organelles	n = 1.38-1.41
Membrane	n = 1.46 (1.43-1.49)
Collagen	n = 1.46-1.53

Table 1: *Refractive indices for structures likely to be encountered by the Mach-Zehnder beam. Taken from [22]*

At this point it may prove necessary to use ray-tracing algorithms, where the light received at each CCD is traced back along its possible paths until the source is reached [28]. Very efficient ray tracing algorithms exist, though not in Matlab so the computational backend would have to be constructed in a more low-level language such as C++. This class of algorithms are renowned for the photorealistic images they can produce given a 3D model, and thus would be well suited for accurately modelling the light through its media. In complex, living tissue, the scattering is so advanced that probability distributions have to be introduced, and Monte Carlo simulations conducted.

IX. Discussion

The implementation of the algorithms described would be ambitious and far beyond what is possible in the time frame of this short Case Presentation. However, the ideas contained could well be used to expand the proof-of-concept instrument devised by Chen et al. into a sub-nanometric instrument capable of measuring living biological matter.

References

[1] Hell, Stefan W. "Microscopy and its focal switch." Nature Methods 6.1 (2008): 24-32.

[2] Koster, Abraham J., and Judith Klumperman. "Electron microscopy in cell biology: integrating structure and function." Nature Reviews Molecular Cell Biology 4.9; SUPP (2003).

[3] Hahn, Theo, et al. International tables for crystallography. D. Reidel Publishing Company, 2005.

[4] Verkleij, A. J., et al. "Phase transitions of phospholipid bilayers and membranes of Acholeplasma laidlawii B visualized by freeze fracturing electron microscopy." Biochimica et Biophysica Acta (BBA)-Biomembranes 288.2 (1972): 326-332.

[5] Danilatos, G. D. "Introduction to the ESEM instrument." Microscopy research and technique 25.5?6 (2005): 354-361.

[6] Scott, M. C., et al. "Electron tomography at 2.4-angstrom resolution." Nature 483.7390 (2012): 444-447.

[7] Li, Du, and Rose Zou. "Preparation of transmission electron microscope samples." U.S. Patent No. 6,194,720. 27 Feb. 2001.

[8] Ushiki, T., et al. "Atomic force microscopy in histology and cytology." Archives of histology and cytology 59 (1996): 421-432.

[9] Smyth, M. S., and J. H. J. Martin. "x Ray crystallography." Molecular Pathology 53.1 (2000): 8-14.

[10] Li, Enbang, Kiet Tieu, and Mark Mackenzie. "Interference patterns of two focused Gaussian beams in an LDA measuring volume." Optics and lasers in engineering 27.4 (1997): 395-407.

[11] Tolansky, S. "Interferometry and biological microtopography." Journal of Theoretical Biology 5.2 (1963): 306-320.

[12] McDonald, Kirk T. "Reflection of a Gaussian Optical Beam by a Flat Mirror."

[13] Self, Sidney A. "Focusing of spherical Gaussian beams." Applied optics 22.5 (1983): 658-661.

[14] Hendrickson, Wayne A. "X rays in molecular biophysics." (1995).

[15] Pawley, James, ed. Handbook of biological confocal microscopy. Springer, 2006.

[16] Zhang, Jin, et al. "Creating new fluorescent probes for cell biology." Nature Reviews Molecular Cell Biology 3.12 (2002): 906-918.

[17] Hariharan, Parameswaran. Optical Interferometry, 2e. Academic Press, 2003.

[18] Su, Der-Chin, Ming-Horng Chiu, and Cheng-Der Chen. "A heterodyne interferometer using an electro-optic modulator for measuring small displacements." Journal of Optics-Nouvelle Revue d 'Optique 27.1 (1996): 19-24.

[19] Wyatt, T. "CP1: Investigation into the feasibility of a Three Axis Interferometer for Biological Microscopy." UCL CoMPLEX Case Presentation (2012)

[20] Mishina, Hiromichi, and Toshimitsu Asakura. "Two gaussian beam interference." Nouvelle Revue d 'Optique 5.2 (2002): 101.

[21] Barone, Fabrizio, et al. "Fringe-counting technique used to lock a suspended interferometer." Applied optics 33.7 (1994): 1194-1197.

[22] Nolte, David D. Optical interferometry for biology and medicine. Springer, 2011.

[23] Chen, Benyong, Xiaohui Cheng, and Dacheng Li. "Dual-wavelength interferometric technique with subnanometric resolution." Applied optics 41.28 (2002): 5933-5937.

[24] Poon, Ting-Chung, and Partha P. Banerjee. Contemporary optical image processing with MATLAB. Elsevier Science, 2001.

[25] He, Liangfang. "Vibration-compensated interferometry system using phase-modulating interference fringe subdivision technology." Applied optics 45.31 (2006): 7987-7992.

[26] Robinson, David W. "Automatic fringe analysis with a computer image-processing system." Applied Optics 22.14 (1983): 2169-2176.

[27] Hu, Lifa, et al. "Phase-only liquid crystal spatial light modulator for wavefront correction with high precision." Optics Express 12.26 (2004): 6403-6409.

[28] Glassner, Andrew S. An introduction to ray tracing. Morgan Kaufmann, 1989.